A Methodology for Remote Sensing Inter-Turn Fault Events in Power System Air-Core Reactors, via Simulation of Magneto Quasi-Static Fields in 2D FDTD

ATA ZADEHGOL (Sr. Member, IEEE), HANGTIAN LEI (Member, IEEE), and BRIAN K. JOHNSON (Sr. Member, IEEE)

Electrical and Computer Engineering, University of Idaho, Moscow, ID 83843 USA (e-mail: azadehgol@uidaho.edu)

Corresponding author: Ata Zadehgol (e-mail: azadehgol@uidaho.edu).

ABSTRACT We present a numerical methodology to estimate the transient fault currents and to simulate the remote sensing of transient fault information embedded in the magnetic field emissions caused by inter-turn shorts in 60 Hz air-core reactors, thru a magneto quasi-static (MQS) field approximation in the method of Finite-Difference Time-Domain (FDTD) in 2-dimensional (2D) space. The MQS 2D FDTD fields of reactor in normal operation are scaled by correlation against an equivalent circuit model that is derived from application of basic physics principles to parameters of the 3D air-core reactor. The proposed multi-scale quasi-static modeling methodology, based on the *reduced c* modification, provides fine-feature access down to the single-wire level and can efficiently estimate the transient fault fields and currents due to turn-to-turn short in a reactor with core height in several meters, core diameter in meters, wire diameter in millimeters, and number of turns in the thousands, at 60 Hz; this is accomplished by using computational resources of a typical laptop computer within *seconds* or *minutes*, as opposed to *days* that would be otherwise required without the *reduced c* modification.

INDEX TERMS Air-core reactor, inter-turn fault, inter-winding fault, magneto quasi-statics, transient fault, turn-to-turn fault.

I. INTRODUCTION

THE air-core reactor [2] is primarily used as a current limiting device across power networks around the world. It is comprised of coils of wire wound around a hollow cylindrical dielectric (e.g., PVC in the lab, or frame in the field) with air for its core material, as depicted in Fig. 1. To achieve the same level of inductance in lieu of a magnetic core (such as iron-core), an air-core reactor needs many more wire turns than its magnetic-core counterpart. Iron core reactors are filled with dielectric oil, while air-core reactors are seeing increased use in environmentally sensitive areas. Turn-to-turn faults involving a small number of turns are difficult to detect in air-core reactors, due to the limited voltage drop per turn. Methods applied based on voltage or current measurements to detect faults in iron-core reactors have limited sensitivity to fault detection in air-core reactors [3], [4]. A 2D cross-sectional view in Fig. 2 shows the structure during normal operation, where the parameters of a typical air-core reactor in the field can span a range of values; a reasonable estimate is given in Table 1 [5], [6].

If the dielectric insulation of the wires break (e.g., due to overheating, environmental conditions, etc.) and the winding conductors are exposed to form an inter-turn electric short as depicted in Fig. 3, then a small initial fault current can evolve over time to cause more significant damage to the reactor, requiring it to be removed from service.

Previous investigators have proposed models and methods for detecting the fault current due to inter-turn short (also called an inter-winding or turn-to-turn short). For example, the work by [4], [7] relied primarily on experimental measurements of electrical quantities (e.g., voltage, current) in laboratory, validated by simulations of circuit models [4],

[7]. The work by [8] performed simulations of equivalent circuit models based on the finite element method (FEM) to study the frequency-domain variations in spatial distribution of magnetic field.

An independent, but somewhat related, area in power networks that often requires electromagnetic modeling and analysis of solenoids is the *rotating machines* which have been the subject of a lot more analysis [9]–[12] due to their existence in much larger quantities and their higher economic value. Although, reactors and rotating machines are devices with different dimensions and applications, previous works may provide useful insights about the state of computational electromagnetic (CEM) modeling in dense coils of wiring, at 60 Hz. For example, the work by [13] performed fault analysis of motors using a CEM software based on 2D FEM, where each coil has 26 turns and turn-to-turn fault is induced by shorting 6 turns. The work by [14] developed a phase variable model of machines based on FEM combined with wavelet analysis, to predict turn-to-turn short circuit fault, and applied it to a 2-hp/6-pole/36-slot motor where up to 3 turns are shorted.

Our main contribution in this work is to develop an efficient time-domain CEM modeling methodology to sense inter-turn faults based on transient magnetic field emissions, rather than using voltage or current quantities. More specifically, we present a modeling and simulation methodology to remote-sense the transient fault information embedded in the magnetic field emissions, due to inter-winding shorts in air-core reactors with realistic parameters specified in Table 1, where core height is in several meters, core radius is in meters, wire diameter is in millimeters, and number of wire turns is in the thousands. The estimate is computed within seconds or minutes, using computational resources of only a typical laptop computer. The time-domain CEM model is implemented in the method of finite-difference time-domain (FDTD) in the magneto quasi-static (MQS) regime, with fine spatial resolution that provides access to the smallest feature (single-wire) all the way to the largest feature (core height) in one model. We believe the proposed methodology for modeling transient fault events in air-core reactors is unique and has not been presented in the literature previously, to the best of our knowledge.

We develop the proposed modeling methodology in the remainder of this paper which is organized as follows. In *Section II*, we provide an overview of the essential challenges in using the original FDTD algorithm to solve the electromagnetic (EM) fields of a *multi-scale* and *quasi-static* problem. In *Section III-A*, we rely on basic physics principles to develop an approximate equivalent circuit model of the 3D reactor structure. In *Section III-B*, we define the excitation current source as a Gaussian pulse with a 60 Hz half-bandwidth at -3 dB, and derive the time-domain voltage response of the equivalent circuit model for later use in correlation and scaling of the FDTD model. In *Section III-C*, we apply the *reduced c* method, through modification of free-space permittivity ϵ_0, to the standard Yee FDTD algorithm

and obtain an MQS 2D FDTD model to estimate the electric field $\vec{E}(t, x, y)$ and magnetic field $\vec{H}(t, x, y)$ in 2D space (in the x-y plane) as a function of time t (s). In *Section III-D*, we use the voltage and current approximations from the circuit model in normal operation to scale and correlate the mathematical EM fields from the MQS 2D FDTD model. In *Section IV-A*, we correlate the FDTD model against the equivalent circuit model via several numerical experiments. In *Section IV-B*, we simulate the transient fault currents on inter-winding shorts, and in *Section IV-C*, we demonstrate the proposed modeling methodology by computing the time-varying magnetic field emissions to simulate remote sensing a transient fault event in the reactor of Table 1. We conclude with closing remarks in *Section V*.
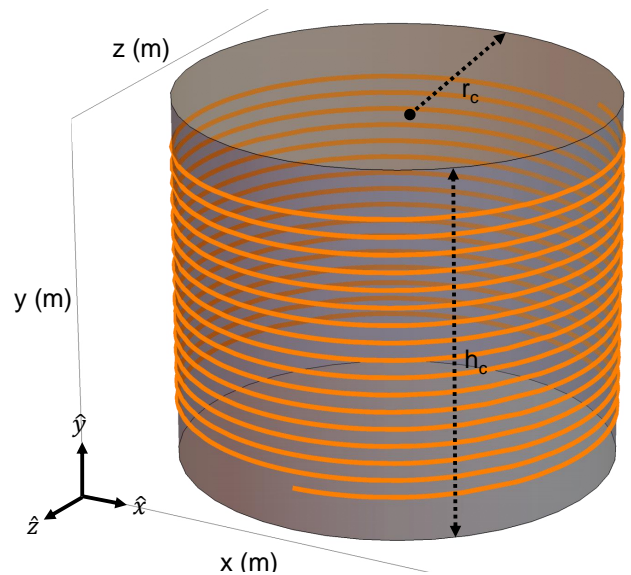
FIGURE 1. Conceptual view of a typical 3D reactor with air core (hollow gray cylinder) and winding wire conductors (orange lines), where core radius is r_c and core height is h_c. This is a conceptual perspective because the parameter scales were chosen to make distinct wires, with d_w in millimeters, visible relative to the entire core with r_c and h_c in meters.

II. FDTD FOR MULTI-SCALE & QUASI-STATIC REGIME

Given that 60 Hz is a relatively low frequency, it may be tempting to pursue a *static* solution; however, such a solution is inadequate for quantifying the *transient* nature of the fault currents and fields. The structure depicted in Fig. 2 with parameter values specified in Table 1 does not lend itself easily to Yee's original FDTD method [15]–[17] for solving the *transient* EM fields, due to its *multi-scale* and *quasi-static* nature; as explained below.

There is significant spatial disparity between the structure's size and the operational wavelength. Specifically, the smallest feature of the structure ($d_w = 4.12$ mm) is about nine orders-of-magnitude smaller than the operational wavelength ($\lambda_0 = 5000$ km). In addition, the smallest feature is about three orders-of-magnitude smaller than the largest feature ($h_c \cong 3 - 8$ m) that further increases the computational burden when using a uniform grid, since the bottleneck on
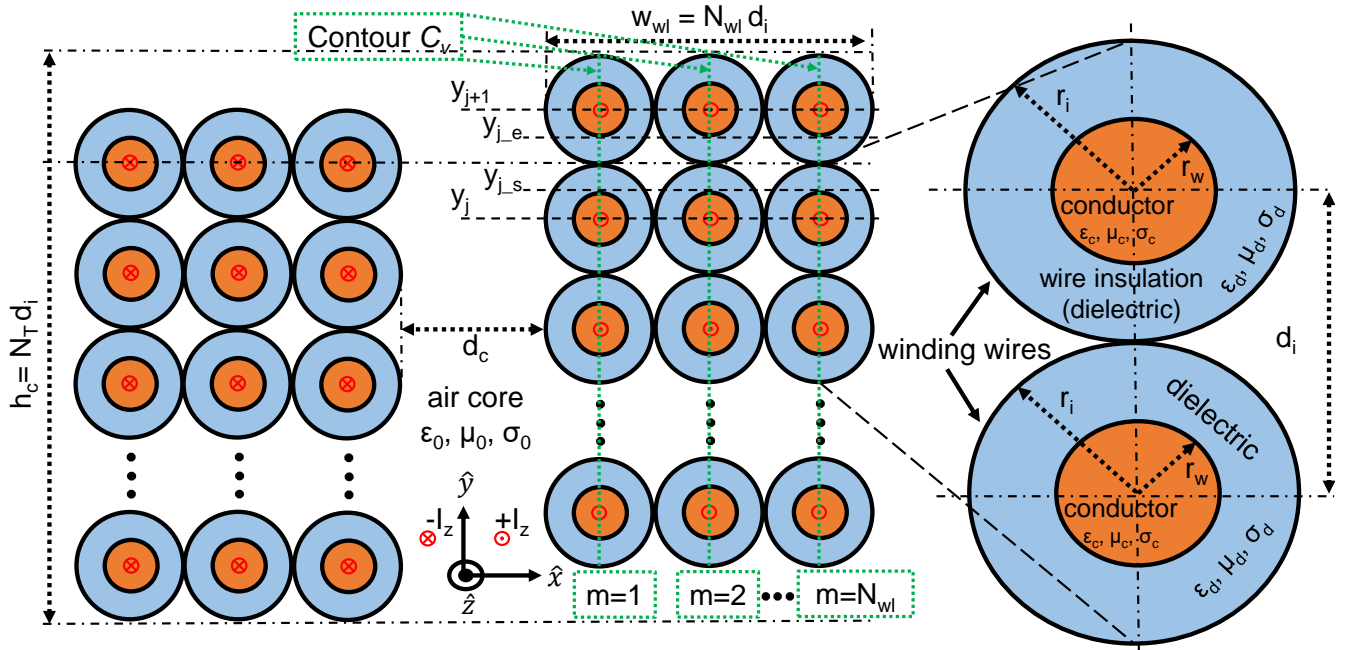
FIGURE 2. A 2D cross-section view of an air-core reactor. The core height is along the y-axis and the winding wire conductors (orange disks) carry current I_z along the z-axis. d_c is the diameter of the core, h_c is the height of the core, N_T is the number of turns, N_{wl} is the number of winding layers, w_{wl} is the total width of the winding layers along the x-axis, r_w is the radius of the wire's conductor, r_i is the radius of the wire's dielectric insulation (blue disks), d_i is the pitch (center-to-center distance) of two nearest wires. The permittivity, permeability, and conductivity of the material is given respectively for the conductor $\{\epsilon_c, \mu_c, \sigma_c\}$, for the insulation dielectric $\{\epsilon_d, \mu_d, \sigma_d\}$, and for the air core $\{\epsilon_0, \mu_0, \sigma_0\}$. Unit vectors in the Cartesian coordinate system are $\{\hat{x}, \hat{y}, \hat{z}\}$. The $\int_C \vec{E}.d\vec{l} = V$ is integrated along the contour C_v, parallel to $\hat{y}$ at each index m along $\hat{x}$, to compute the voltage V_{coil} across terminals of the coil with N_T turns.

Parameter	Value Range	Comments
r_w	2.06 (mm)	6 AWG, radius
d_w	4.12 (mm)	6 AWG, diameter
λ_0	5000 (km)	Wavelength of operation
f_0	60 (Hz)	Frequency of operation
r_i	$2 \times r_w$	
d_i	$2 \times r_i$	
N_{wl}	2 - 3	
w_{wl}	$N_{wl} \times d_i$	along $\hat{x}$
N_T	300 - 1000	per wl
h_c	$N_T \times r_i$	along $\hat{y}$
r_c	1 - 2 (m)	along $\hat{x}$
d_c	$2 \times r_c$	along $\hat{x}$
N_s	1-100	along $\hat{y}$
h_s	$N_s \times d_i$	along $\hat{y}$
w_s	$\leq w_{wl}$	along $\hat{x}$
I_z	300 - 1000 (A) RMS	$\pm I_z$ is along $\pm \hat{z}$
I_0	1400 (A)	peak value of I_z
σ_c	5.8×10^7 (S/m)	Copper
ϵ_0	8.842×10^{-12} (F/m)	
ϵ_d	$4.0 \times \epsilon_0$	PVC
σ_d	0.0001 (S/m)	PVC
σ_0	$5 \times 10^{-15} \approx 0$ (S/m)	at 20° C
μ_0	$4\pi \times 10^{-7}$ (H/m)	
μ_d, μ_c	μ_0	

TABLE 1. Table of parameter values for a typical air-core reactor. Usually in the field for a 3-phase 60 (Hz) power system, three such reactors are connected in a linear or triangular alignment. We define the nominal parameter values as $N_T = 1000$, $r_c = 1.0$ m, $I_0 = 1.0$ A, $\epsilon_d = \epsilon_0$, $\sigma_d = \sigma_0$, and $N_{wl} = 1$; unless otherwise explicitly stated, the nominal values are assumed throughout this paper.
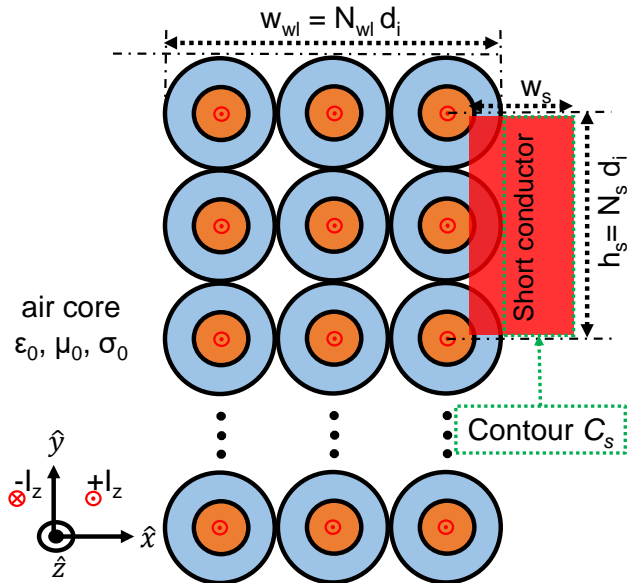
FIGURE 3. Fault current can be induced if wire conductors (orange disks) are shorted (red rectangle) across layers or within a layer. This can occur by wear-out in wire insulation due to repeated surges, environmental effects, etc. Ampere's law $\oint_C \vec{H}.d\vec{l} = I$ is integrated along the closed contour C_s to compute the fault current on the short conductor.

the spatial discretization of the largest feature (h_c) is dictated by the smallest feature (d_w).

In pursuit of a transient solution, starting with the standard

Yee's 2D FDTD method, a typical spatial discretization based purely on wavelength, may be $\Delta x = \lambda_0/20 = 250$ km [18]; however, our goal of modeling inter-turn shorts requires access to the single-wire level, and a Δx in kilometers clearly fails to provide sufficient spatial resolution for sampling each wire in millimeters. A more reasonable choice for Δx may be some fraction of the wire diameter; e.g., $\Delta x = d_w/4 = 1.03$ mm; however, considering the Courant stability criteria (i.e., $\Delta t < \frac{\Delta x}{\sqrt{2}c_0}$ (s), where speed of light in vacuum is $c_0 \cong 3.0 \times 10^8 = 3.0$E+8 m/s), that choice of Δx dictates an extremely small $\Delta t = 2.43$ ps. Considering that at 60 Hz, one period $T_0 = 1/f_0 \cong 16.667$ ms, it would require approximately 6.87E+9 time-steps to simulate the response to just one period T_0 of a time-harmonic excitation; that is an enormous number of time iterations which exerts increasingly exorbitant computational costs across 1D, 2D, and 3D FDTD on any ordinary, yet respectable, workstation computer today.

The issue of massive time-iterations in the quasi-static regime, due to tiny temporal discretization Δt in the Courant-constrained central-difference based FDTD, has been studied by previous investigators [19]–[24] for various other applications. The basic idea is that at low frequencies (e.g., 60 Hz) where the wavelength is extremely large compared to the (electrically small) structure's size, the wave's propagation-time across the characteristic length of the structure is much smaller than the time period of interest T_0 (i.e., $h_c/c_0 \ll T_0$) [25]; yielding conditions that are suitable for *quasi*-static approximation of Maxwell's ($\nabla \times \vec{E}$ and $\nabla \times \vec{H}$) equations which, under the above circumstances, are *weakly* coupled, or *almost* (but *not completely*) decoupled.

An interesting idea, called *reduced c*, was proposed by previous investigators [19]–[21] for various different applications, where the free-space material properties are modified to reduce the propagation velocity and thereby increase Δt closer in order-of-magnitude to T_0. For this paper, we utilize the *reduced c* method, due to its relative simplicity and convenience in requiring minimal modification to the original Yee's FDTD algorithm.

The 2D FDTD simulation results presented in section III, section IV-A, and section IV-B were generated using a fairly typical (by today's standards) laptop computer running 64-bit Linux [26] operating system on a dual-core CPU [27] and random access memory (RAM) of 24.0 GB. Each 2D FDTD simulation that was run at the *fine* (*coarse*) sampling corner in the range of spatial (8) and temporal (9) discretization, generally took *minutes* (*seconds*) to estimate the EM fields of the nominal 2D air-core reactor in Table 1; in contrast, without the *reduced c* modification each FDTD simulation run would have required *days* to complete.

III. FORMULATION

A. EQUIVALENT CIRCUIT MODEL

The circuit model is derived from basic physics principles and the 3D parameters of air-core reactor in Fig. 1 and Table 1. Each loop of the coil may be modeled as an equivalent circuit comprised of a resistor in series with an inductor [28], where R_{p_m} (Ω) is the resistance per loop (1), and L_{p_m} (H) is the inductance per loop (2); the winding layer number is designated by the subscript index $m \in \{1, 2, 3, \dots\}$. Internal inductance of the wire is considered negligible here, and thus ignored.

$$R_{p_m} = R_{\text{pul}}2\pi \left(r_c + r_i + (m-1)d_i\right), \qquad (1)$$

where the resistance per-unit-length (pul) of the wire is defined as $R_{\text{pul}} = 1/(\sigma_c \pi r_w^2)$ (Ω/m).

$$L_{p_m} = \frac{N_T}{h_c}\mu_0\pi \left(r_c + r_i + (m-1)d_i\right)^2 \qquad (2)$$

Subsequently, the impedance Z_{coil} (Ω) across terminals of the entire coil in normal operation, with N_T turns and N_{wl} winding layers, may be obtained by

$$Z_{\text{coil}}(\jmath\omega) = N_T \sum_{m=1}^{N_{wl}} \left(\jmath\omega L_{p_m} + R_{p_m}\right), \qquad (3)$$

where the imaginary number $\jmath = \sqrt{-1}$, the angular frequency $\omega = 2\pi f$ (rad/s), and the cyclic frequency is f (Hz).

B. CURRENT SOURCE EXCITATION, AND VOLTAGE RESPONSE

The reactor model is excited by an ideal current source that has a Gaussian pulse waveform with a 60 Hz half-bandwidth at -3 dB, and a peak value of I_0 (A), given by

$$I_{\text{source}}(t) = I_0 e^{\frac{-(t-t_{\text{pk}})^2}{2t_{\text{sp}}^2}}, \qquad (4)$$

where t_{pk} is the time at which the pulse peak occurs, and t_{sp} is the pulse time-spread. To achieve a 60 Hz half-bandwidth at -3 dB from the peak, we set $t_{\text{sp}} = 2.20$ ms while ensuring t_{pk} is greater than approximately $5t_{\text{sp}}$; i.e., $t_{\text{pk}} \gtrsim 11.0$ ms. Given that in our case, skin-effect [29] is negligible (i.e., at 60 Hz, copper has a skin depth $\delta_s \cong \sqrt{2/(\omega\mu\sigma)} = 8.53$ mm $> d_w$), the source current may be approximated to have a uniform distribution across each wire's conductor region.

Multiplying the Fourier transform of (4) by (3), then taking the inverse Fourier transform of the product [30], yields the time-domain voltage response (5) of the entire coil to the Gaussian pulse excitation in normal operation.

$$
\begin{aligned}
V_{\text{coil}}(t) = {}& -N_T I_0 e^{-\frac{(t-t_{\text{pk}})^2}{2t_{\text{sp}}^2}} \\
& \times \sum_{m=1}^{N_{wl}} \left(((t_{\text{pk}} - t)/t_{\text{sp}}^2)L_{p_m} + R_{p_m}\right) \quad (5)
\end{aligned}
$$

C. MAGNETO QUASI-STATIC (MQS) APPROXIMATION

Assuming an infinitely long wire in the $\hat{z}$ direction and a source current having only a z-component $I_z(\rho)$ flowing along $\hat{z}$, permits a 2D approximation where it is convenient to assume z-invariance (i.e., $\frac{\partial}{\partial_z} = 0$) to formulate a transverse-magnetic-to-z (TM^z) problem [29] with the z-component of H-field $H_z = 0$; this approximation eliminates three field components E_x, E_y, H_z and one spatial variable z, and leads

to the modified Maxwell's equations (6) with only three non-zero field components E_z, H_x, H_y, where the electric field has only a z-component E_z along $\hat{z}$, and the magnetic field possess only an angular component H_ϕ along $\hat{\phi}$ [29].

$$\nabla \times \vec{E}(t,x,y) = -\frac{\partial}{\partial t}\vec{B}(t,x,y),$$

$$\nabla \times \vec{H}(t,x,y) = \frac{\partial}{\partial t}\vec{D}(t,x,y) + \vec{J}(t,x,y), \quad (6)$$

where $\vec{E} = \{\hat{z}E_z(t,x,y)\}$ (V/m), $\vec{J} = \{\hat{z}J_z(t,x,y)\}$ (A/m²), $\vec{H} = \{\hat{x}H_x(t,x,y), \hat{y}H_y(t,x,y)\}$ (A/m) in rectangular coordinates or $\vec{H} = \{\hat{\phi}H_\phi(t,\rho)\}$ (A/m) in cylindrical coordinates, the electric flux density $\vec{D} = \epsilon_0\epsilon_r\vec{E}$ (coulombs/m²), ϵ_r is the relative permittivity of the medium, and the magnetic flux density $\vec{B} = \mu_0\vec{H}$ (webers/m²).

For the purposes of this work, an electromagnetic modeling approach in 2D space was presumed sufficient, and preferred over a 3D approach which would substantially increase computational costs. The 2D environment assumes that the inter-winding short conductor is a rectangular slab laid in the x-y plane that extends infinitely along $\hat{z}$, and induces a transient fault current along $\hat{z}$ that is attributed to the magnetic field components H_x, H_y (or H_ϕ along $\hat{\phi}$).

The 1st order coupled partial differential equations (6) are reduced to the magneto quasi-static (MQS) approximation [25]

$$\nabla \times \vec{E}(t,x,y) = -\frac{\partial}{\partial t}\vec{B}(t,x,y),$$

$$\nabla \times \vec{H}(t,x,y) \cong \vec{J}(t,x,y), \quad (7)$$

where the free-space permittivity ϵ_0 is scaled by $S_\epsilon = 5.0\text{E}+7$ and revised to $\epsilon_{0_s} = \epsilon_0 S_\epsilon$ [19], [20] to enable the approximation $\frac{\partial}{\partial t}\vec{D}(t,x,y) \cong 0$; this implies a relatively negligible contribution from the electric displacement current.

The MQS approximation (7) is implemented in 2D FDTD. Furthermore, it was found that uniform spatial discretization in the range of (8) provides sufficient spatial resolution. Considering the Courant stability criteria in 2D FDTD, that choice of Δx leads to uniform temporal discretization in the range of (9) across each time-step n.

$$\Delta x = d_w/\Delta_{d_w} \quad (8)$$
$$= \Delta y \in [d_w/4 = 1.03 \text{ mm}, d_w/8 = 0.515 \text{ mm}]$$

$$\Delta t \in [0.0605 \text{ ms}, 0.121 \text{ ms}] \quad (9)$$

Given the goal of this work is to present a CEM modeling methodology for numerical estimation of the transient fault currents and remote-sensing transient fault events due to inter-winding shorts in air-core reactors, further details of formulation and implementation of MQS equations in 2D FDTD fall outside the scope of the present paper; however, those details may be submitted as a separate publication in the future.
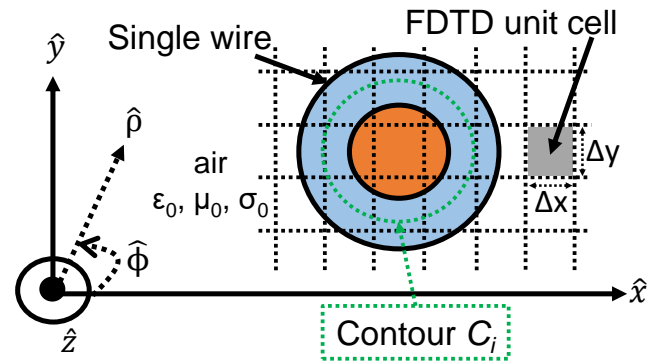
FIGURE 4. 2D FDTD rectangular grid with uniform spatial discretization $\Delta x = \Delta y$. Ampere's law integration $\oint_C \vec{H}.d\vec{l} = I$ is performed around the closed contour C_i to compute the current I_z along a single wire conductor (orange disk). Unit vectors in the cylindrical coordinates are $\{\hat{\rho}, \hat{\phi}, \hat{z}\}$.

D. SCALING V, I FROM MQS 2D FDTD

In Fig. 5, we compare the voltage and current from MQS 2D FDTD vs. the equivalent circuit model. As can be observed, the normalized (*relative*) version of voltage waveforms in Fig. 5(a),(b) are in good agreement; a similar assessment is made of the normalized (*relative*) version of current waveforms in Fig. 5(c),(d). However, in *absolute* terms, there is about five orders of magnitude discrepancy in voltage amplitude values between the un-scaled MQS 2D FDTD solution vs. the equivalent circuit solution. The amplitude discrepancy across scaled vs. un-scaled plots of the current appear to be less significant than that of the voltage; however, the current is computed for one single wire turn of the coil, while the voltage is computed across all N_T wire turns of the coil.
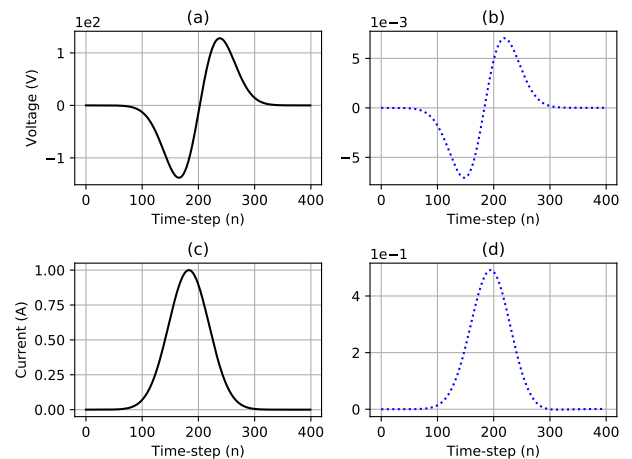
FIGURE 5. Un-scaled voltage (b) and current (d) from MQS 2D FDTD vs. voltage (a) and current (c) from equivalent circuit. Reactor parameters are set to nominal values in Table 1.

1) Scaling Current from MQS 2D FDTD
Ampere's law [18], [29] may be applied to the H-field computed in FDTD to find the current I_z through the line integral

of $\vec{H}$ along a closed contour C_i around a single wire; i.e., $\oint_C \vec{H}.d\vec{l} = I_z$, see Fig. 4. The current I_{z3} is computed along contour of radius $3 \times r_w$ from center of a single wire. The MQS 2D FDTD current solution I_{FDTD} may be scaled to the equivalent circuit solution $I_{FDTD_{scaled}}$, by using the current scaling factor S_I in

$$I_{FDTD_{scaled}} = I_{FDTD}S_I, \quad (10)$$

where S_I is a constant based on assumptions in the MQS 2D FDTD; e.g., in this case for nominal parameter values of Table 1, it is empirically determined that $S_I \cong 2.0$. Scaled current results are shown in Fig. 6, where I_s was aligned with the curve of $r_w = 0.81$ mm for reference; notice a slight time-delay that increases with increasing r_w, given that the integration contour radius increases with r_w. Additional small discrepancies may be due to approximating a circular contour in a rectangular FDTD grid with finite spatial discretization.
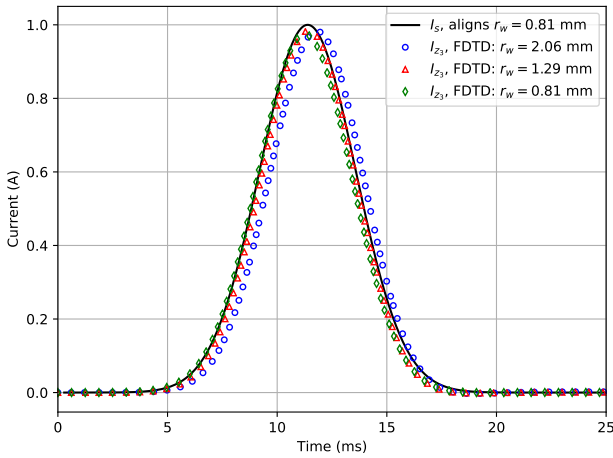
FIGURE 6. Current from equivalent circuit (solid black), and from scaled FDTD (shapes: circle, triangle, diamond). The FDTD current is computed via the Ampere's law integration of the magnetic field ($\oint_C \vec{H}.d\vec{l} = I_z$). The source current is I_s.

2) Scaling Voltage from MQS 2D FDTD

Maxwell-Faraday's law [18], [29] describes the relation between the E-field obtained from FDTD and the voltage V_{yz} through the line integral of $\vec{E}$ on the contour C across terminals of the coil along $\hat{y}$ over N_T turns; i.e., $\oint_C \vec{E}.d\vec{l} = -\frac{\partial}{\partial_t}\iint_S \vec{B}.d\vec{s} = \sum V$, where magnetic flux density $\vec{B} = \mu_0\vec{H}$, and V is the voltage around the closed contour C.

Referring to Fig. 2, the voltage V_{coil} across terminals of the coil with N_T turns, is computed by $\int_C \vec{E}.d\vec{l} = V_{coil}$ along the contour C_v, according to (11). The electric field $\vec{E}_m$, at each winding layer location index m, is integrated in the dielectric region $y \in [y_{j\_s}, y_{j\_e}]$ between two conductors, and summed over N_T wire turns and N_{wl} winding layers.

$$V_{coil}(t) = \sum_{m=1}^{N_{wl}}\sum_{j=1}^{N_T}\int_{y_{j\_s}}^{y_{j\_e}}\vec{E}_m(t).d\vec{l}, \quad (11)$$

where j is the location index of position y, and integration for each wire turn begins at y_{j_s} and ends at y_{j_e}.

The MQS 2D FDTD voltage solution V_{FDTD} may be scaled to the equivalent circuit solution $V_{FDTD_{scaled}}$ by using the voltage scaling factor S_V in (12), with S_V given in (13), wherein the assumption $d_c \gg r_w$ is implicit.

$$V_{FDTD_{scaled}} = V_{FDTD}S_V \quad (12)$$

$$S_V = \alpha(\Delta_{d_w})\kappa(r_w)d_c^2, \quad (13)$$

where $\Delta_{d_w} = d_w/\Delta x$, and functions $\alpha(\Delta_{d_w})$ and $\kappa(r_w)$ are coefficients dependent on assumptions in the MQS 2D FDTD, and empirically determined through numerical experiments. Fixing the reactor at the nominal values in Table 1 and making iterative runs thru $r_w \in \{0.81\ mm, 1.29\ mm, 2.06\ mm\}$, we find κ may be approximated by (14) as a sum of powers of $\frac{1}{r_w}$; subsequently, making iterative runs thru $\Delta_{d_w} \in \{4, 8, 12\}$, we find α may be approximated by (15) as a linear function of Δ_{d_w}.

$$\kappa(r_w) \cong 1248.64 + \frac{5.343}{r_w} + \frac{2.752E\text{-}3}{r_w^2} - \frac{1.063E\text{-}6}{r_w^3} \quad (14)$$

$$\alpha(\Delta_{d_w}) \cong 0.2504 + 0.0939\Delta_{d_w} \quad (15)$$
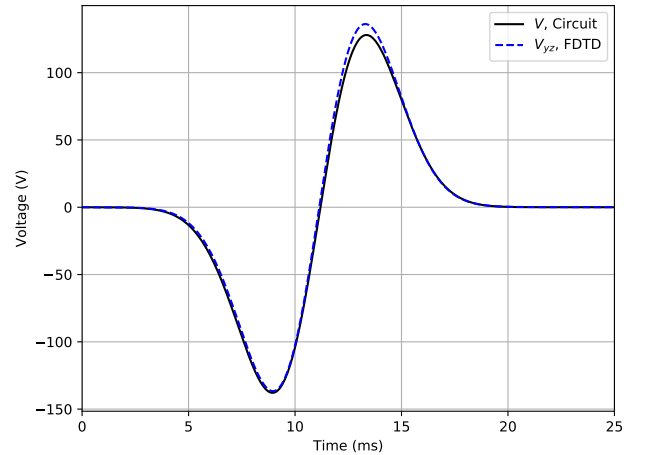
FIGURE 7. Voltage from equivalent circuit (solid black), and from scaled FDTD (dashed blue). Reactor parameters are set to nominal values in Table 1.

The scaled FDTD voltage result is shown in Fig. 7, where the FDTD solution slightly overshoots the equivalent circuit solution; this may be explained by a lower overall inductance and resistance implicit in the 2D FDTD assumptions, compared to the equivalent circuit solution which was derived based on 3D reactor parameters.

Note that the current scaling factor S_I in (10) is a constant, and for fixed values of Δ_{d_w}, r_w, d_c the voltage scaling factor (13) is also a constant. We assume that the scaling factors are independent of the operation mode, whether normal or faulty; thus, we determine the scaling factors under normal

reactor operation and use them to predict the fault currents under inter-winding short conditions.

Although a relatively simple equivalent circuit model, based on 3D reactor parameters, was used here to scale the mathematical EM fields from the MQS 2D FDTD model, one may instead use measurements of an actual air-core reactor, in the laboratory or on the field, to scale the MQS 2D FDTD model.

IV. RESULTS
A. CORRELATION OF FDTD MODEL AGAINST EQUIVALENT CIRCUIT MODEL, THRU NUMERICAL EXPERIMENTS IN SIMULATION

With the MQS 2D FDTD simulation model scaled to the equivalent circuit solution, we perform five numerical experiments in which we plot $V_{\text{coil}}(t)$ vs. time t across variations in r_w, N_T, r_c, N_{wl}, and ϵ_d to validate the MQS 2D FDTD model by correlation against the equivalent circuit model.

In the 1$^{\text{st}}$ numerical experiment, we vary the radius of core and plot the voltage while fixing the remaining parameters at nominal values in Table 1; results in Fig. 8 show very good agreement between the FDTD and the equivalent circuit models.
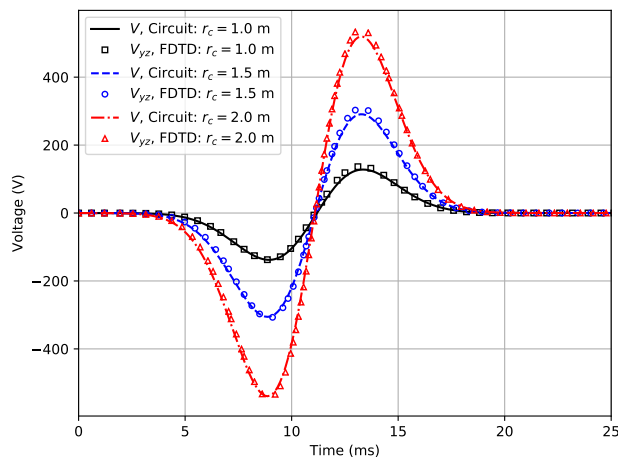
FIGURE 8. Voltage $V_{\text{coil}}(t)$ from equivalent circuit (lines) and from FDTD (shapes), across three values of r_c.

In the 2$^{\text{nd}}$ numerical experiment, we vary the number of turns and plot the voltage while fixing the remaining parameters at nominal values in Table 1; results in Fig. 9 show quite good agreement between the FDTD and the equivalent circuit models.

In the 3$^{\text{rd}}$ numerical experiment, we vary the wire radius and plot the voltage while fixing the remaining parameters at nominal values in Table 1; results in Fig. 10 show good overall agreement between the FDTD and the equivalent circuit models.

In the 4$^{\text{th}}$ numerical experiment, we set $N_{wl} = 3$, vary N_T, and plot the voltage while fixing the remaining reactor parameters at nominal values in Table 1; results in Fig. 11 show reasonable correlation in trends between FDTD and
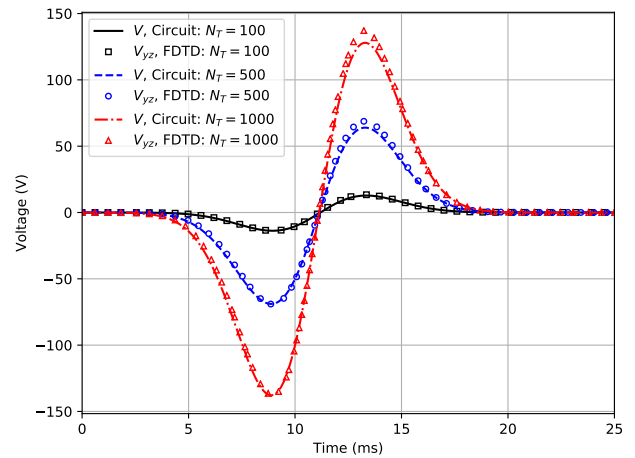
FIGURE 9. Voltage $V_{\text{coil}}(t)$ from equivalent circuit (lines) and from FDTD (shapes), across three values of N_T.
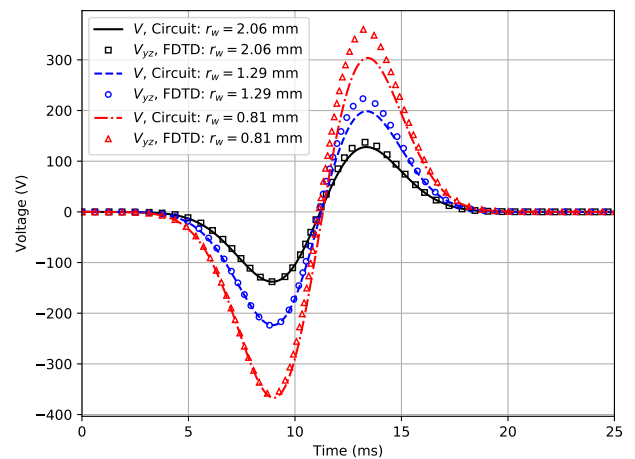
FIGURE 10. Voltage $V_{\text{coil}}(t)$ from equivalent circuit (lines) and from FDTD (shapes), across three values of r_w. Note $r_w = 1.29$ mm (10 AWG) and $r_w = 0.81$ mm (14 AWG) may be useful for correlation against experimental measurements of scaled-down reactor in the laboratory.

equivalent circuit solutions; however, generally the FDTD solution peaks at a higher value and decays faster, compared to its equivalent circuit counterpart.

It's worth noting that any discrepancy in results between the FDTD and the equivalent circuit solutions is likely due to the various simplifying assumptions stated previously, including our rather straightforward approach to developing an equivalent circuit model which was simple, yet sufficient for purposes of this work; however, if required, a 2D FDTD solution may be used with a cellular approach [31] to synthesize a more accurate equivalent circuit model which incorporates both the temporal and spatial characteristics of the reactor more rigorously. Furthermore, a 3D FDTD solution may be attempted if additional accuracy is required; however, at substantially increased computational cost.

In the 5$^{\text{th}}$ numerical experiment, we set ϵ_d and σ_d to PVC, vary r_w, and plot the current while fixing the remaining
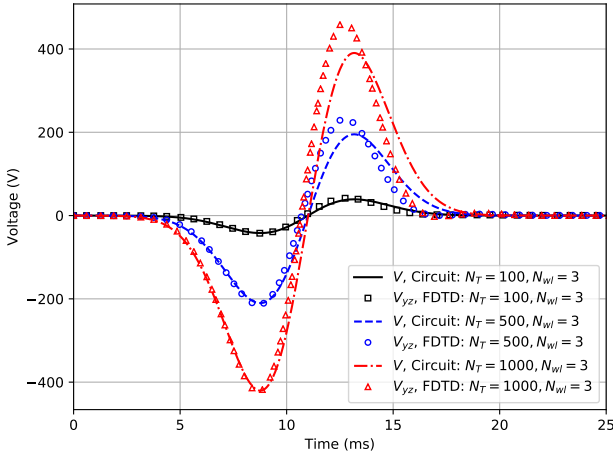
FIGURE 11. Voltage $V_{\text{coil}}(t)$ from equivalent circuit (lines) and from FDTD (shapes). With $N_{wl} = 3$, we vary N_T across $100, 500, 1000$, for a total number of turns equal to $300, 1500, 3000$, respectively.

reactor parameters at nominal values in Table 1; results in Fig. 12 indicate a relatively larger time-delay across increasing r_w compared to Fig. 6, as changing the wire insulation from air (with $\epsilon_r = 1.0$) to PVC (with $\epsilon_r = 4.0$) reduces the wave propagation velocity and increases the capacitance in the dielectric region surrounding each conductor, thereby affecting the temporal and spatial distributions of fields at each time-step n.
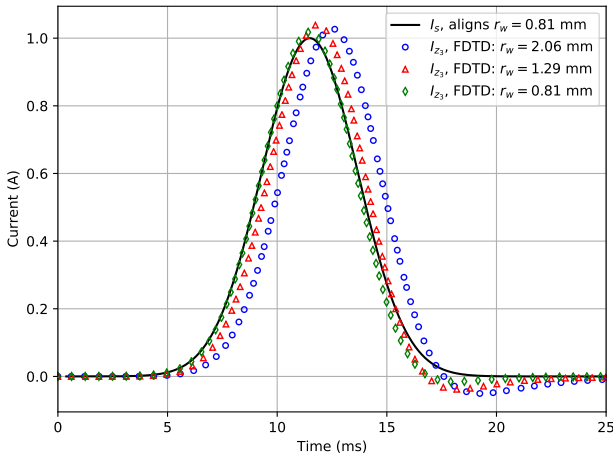
FIGURE 12. Wire insulation material is set to PVC. Current from equivalent circuit (solid black), and from scaled FDTD (shapes). The FDTD current is computed via the Ampere's law integration of the magnetic field ($\oint_C \vec{H}.d\vec{l} = I_z$). The source current is I_s.

B. SIMULATION OF TRANSIENT FAULT CURRENTS IN FDTD

We estimate the transient fault current on the short conductor, in MQS 2D FDTD. Faults are induced by shorting $N_s = \{1, 5, 10, 50, 100\}$ turns respectively, in the middle of the coils vertically along the y-axis. The shorted surface is a rectangular conductive region depicted in Fig. 3 centered

along height of the coil and placed on the right side of reactor. The short current is computed by application of Ampere's law integration $\oint_C \vec{H}.d\vec{l} = I_z$ along the closed contour C_s around the short rectangular conductor. To enable a logical comparison, the current is computed over a fixed area across the five cases of N_s, where the difference between normal vs. faulty current is $\Delta I_z = I_z|_{\text{Faulty}} - I_z|_{\text{Normal}}$; results are shown in Fig. 13 and Fig. 14 for nominal parameters in Table 1. As can be observed, increasing h_s increases ΔI_z; such deviations in the current profile may be exploited to detect a potential fault event due to inter-turn shorts. It is worth noting that direct measurement of the current on the shorted conductor region may not be practical in actual reactor hardware, as the process may be fraught with various technical and safety challenges; instead, we propose remote sensing the fault event through the magnetic field emissions, as described in Section IV-C.
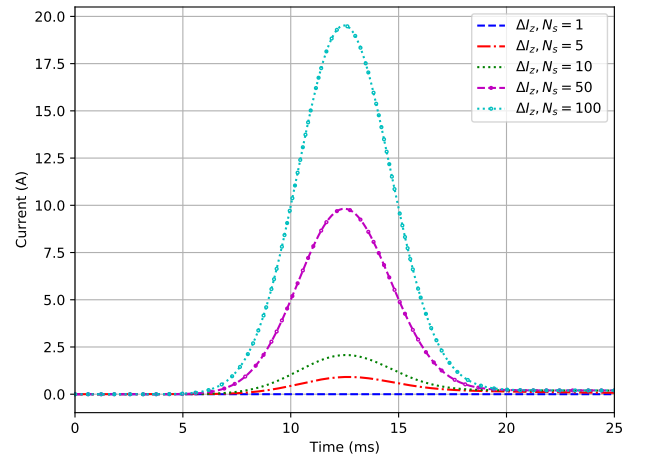
FIGURE 13. The short is a rectangular region with corners at $\{r_c + r_i, -h_s/2\}$ and $\{r_c + r_i + 3r_w, +h_s/2\}$. Current is computed along a fixed rectangular contour region C_s to the right of the wire conductors (see Fig. 3), of width $2r_w$ and height $100d_i$.

C. SIMULATION OF REMOTE SENSING A TRANSIENT FAULT EVENT, THRU COMPUTATION OF THE TIME-VARYING MAGNETIC FIELD EMISSIONS

As a demonstration of the proposed CEM modeling methodology, we compute the time-varying magnetic field emissions to simulate remote sensing a transient fault event caused by inter-turn shorts in an air-core reactor at nominal parameter values given in Table 1. Two sets of MQS 2D FDTD simulations are run, as the time-varying magnetic field is recorded at several points in vicinity of the reactor in Fig. 15; in *set₁* we simulate the reactor under normal operating condition where $N_s = 0$, and in *set₂* we simulate the reactor under transient fault event for five short conditions $N_s = \{1, 5, 10, 50, 100\}$. For each simulation, we record the magnetic field components $\{H_x, H_y\}$ vs. time-step, at the red points depicted in Fig. 15. A similar remote-sensing procedure may be performed by placing magnetic-field sensors near an actual
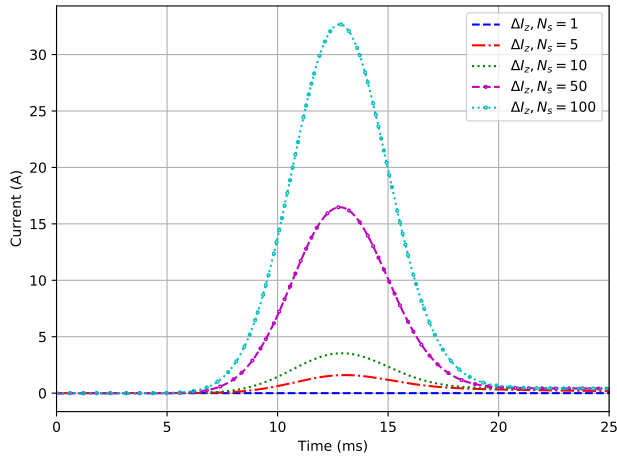
FIGURE 14. The short is a rectangular region with corners at $\{r_c + r_i, -h_s/2\}$ and $\{r_c + r_i + 4r_w, +h_s/2\}$. Current is computed along a fixed rectangular contour region C_s to the right of the wire conductors (see Fig. 3), of width $3r_w$ and height $100d_i$.

reactor in the laboratory or on the field.
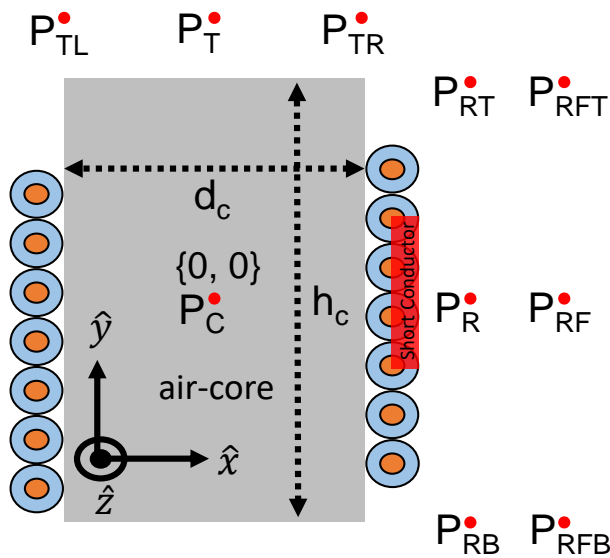
FIGURE 15. Red points indicate the location of H-field sensors relative to center of the air-core (gray rectangle) reactor at point $P_C = \{0, 0\}$, where $P_{RB} = \{r_c + 10r_w, -h_c/2\}$, $P_R = \{r_c + 10r_w, 0\}$, $P_{RT} = \{r_c + 10r_w, h_c/2\}$, $P_{RFB} = \{2r_c, -h_c/2\}$, $P_{RF} = \{2r_c, 0\}$, $P_{RFT} = \{2r_c, h_c/2\}$, $P_{TL} = \{-r_c, h_c/2 + 10r_w\}$, $P_T = \{0, h_c/2 + 10r_w\}$, and $P_{TR} = \{r_c, h_c/2 + 10r_w\}$. The short conductor (red rectangle) has dimensions $d_w \times h_s$ with corners at $\{r_c + r_i, -h_s/2\}$ and $\{r_c + r_i + d_w, +h_s/2\}$; it is inserted on the right to induce transient fault currents.

The results are shown in Fig. 16 thru Fig. 25. Each figure shows the H-field vs. time in solid black for normal operation. The difference between the H-field in normal operation vs. faulty operation (16) is displayed in colored dotted/dashed lines.

$$\Delta H_u = H_u|_{\text{Faulty}} - H_u|_{\text{Normal}}, \qquad (16)$$

where $u \in \{x, y\}$.

Several observations are made: *(1)* as anticipated, clearly there are variations in H-field signal pattern across normal vs. faulty operations, *(2)* in most cases the faulty signal deviates notably from the normal signal at the same time-step and location in space, where the deviations generally increase with N_s, *(3)* in some cases the H-field signal deviations exhibit symmetric behavior across symmetry lines of the reactor; e.g., the sign of ΔH_x flips across the right bottom-to-top (Fig. 17, 18, 19) and across the far right bottom-to-top (Fig. 20, 21, 22), while the sign of ΔH_y flips across left-to-right (Fig. 16, 21), and *(4)* in other cases the H-field signal deviations exhibit asymmetric pattern relative to location of short; e.g., across the top left-to-right (Fig. 23, 24, 25).
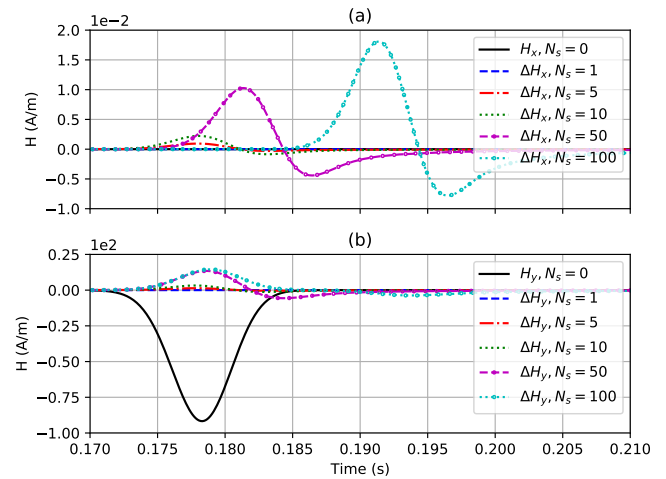
FIGURE 16. (a) H_x, (b) H_y, recorded at the center of reactor, at point $P_C = \{0,0\}$ shown in Fig. 15. In Fig. 16 thru Fig. 25, the solid black line is the H-field value in normal operation, and dotted/dashed colored lines are the change in H-field value across normal and faulty operations defined in (16).
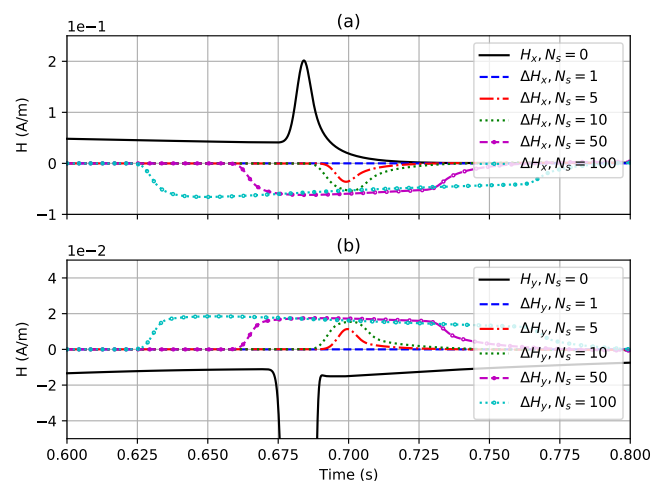
FIGURE 17. (a) H_x, (b) H_y, recorded at right bottom point P_{RB} in Fig. 15.

Finally, we set $N_T = 1000$ and $N_{wl} = 3$ to achieve 3000 total turns, and insert inter-turn short between winding layers $m = 3$ and $m = 2$, as shown in Fig. 26. We repeat the
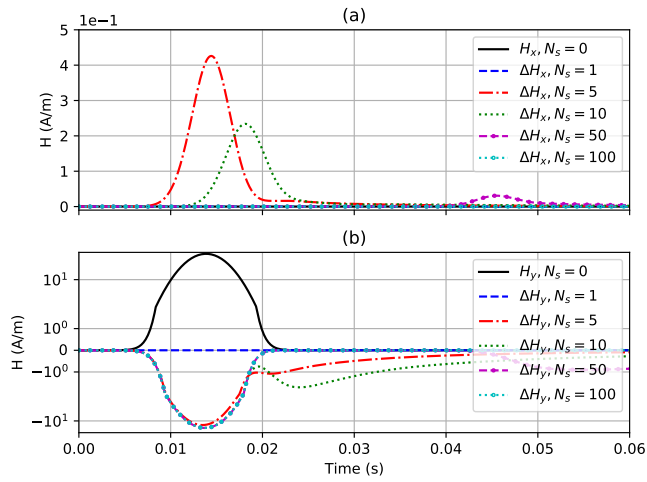
FIGURE 18. (a) H_x, (b) H_y, recorded at the right point P$_R$ in Fig. 15.
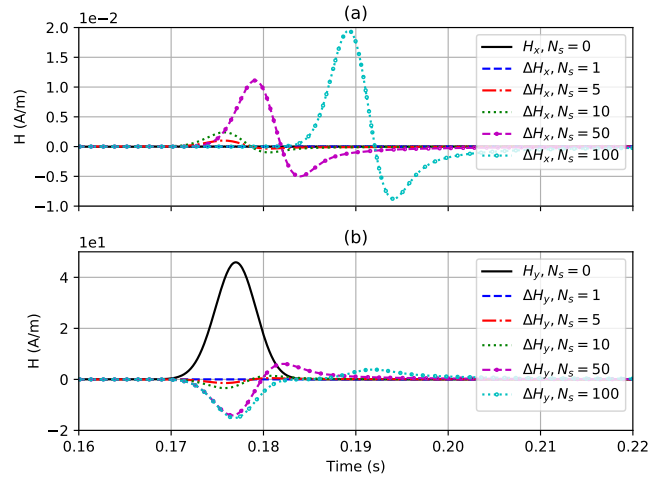
FIGURE 21. (a) H_x, (b) H_y, recorded at far right point P$_{RF}$ in Fig. 15.
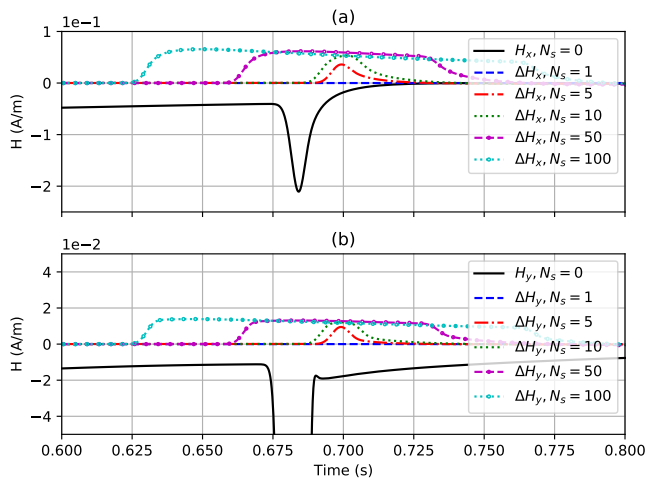
FIGURE 19. (a) H_x, (b) H_y, recorded at right top point P$_{RT}$ in Fig. 15.
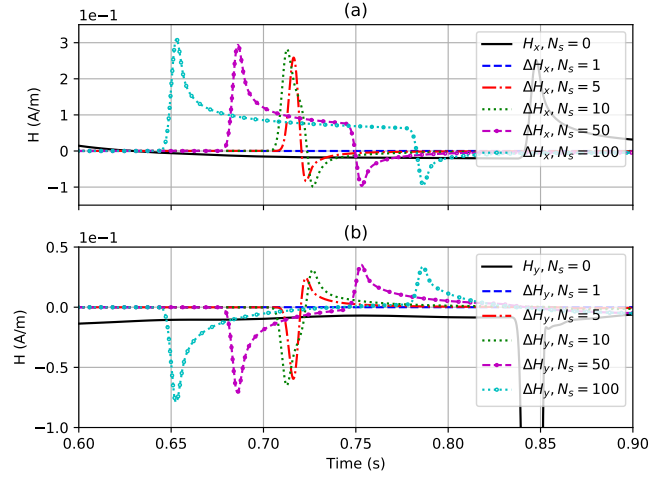
FIGURE 22. (a) H_x, (b) H_y, recorded at far right top point P$_{RFT}$ in Fig. 15.
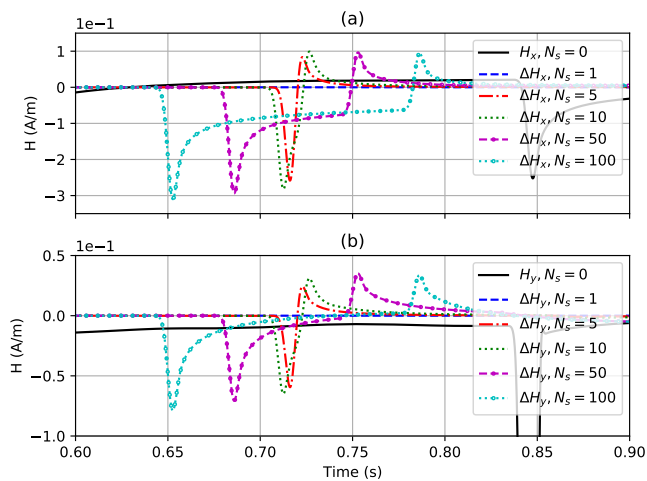
FIGURE 20. (a) H_x, (b) H_y, recorded at far right bottom point P$_{RFB}$ in Fig. 15.
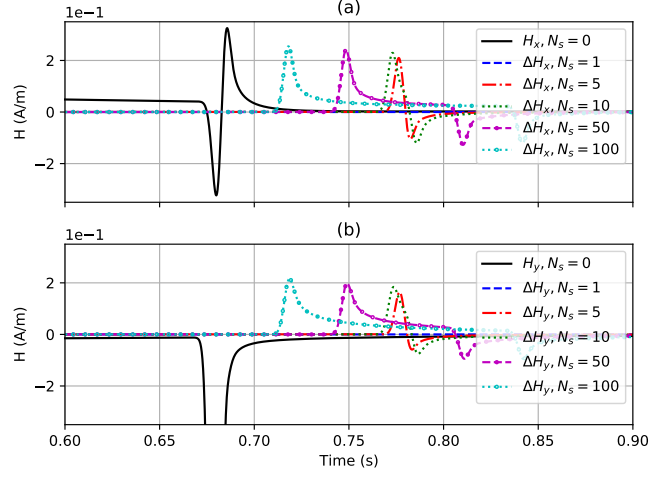
FIGURE 23. (a) H_x, (b) H_y, recorded at top left point P$_{TL}$ in Fig. 15.
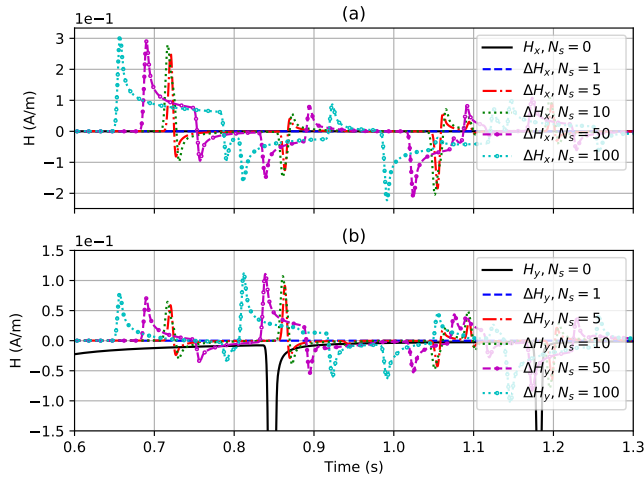
FIGURE 24. (a) H_x, (b) H_y, recorded at top point P$_T$ in Fig. 15.
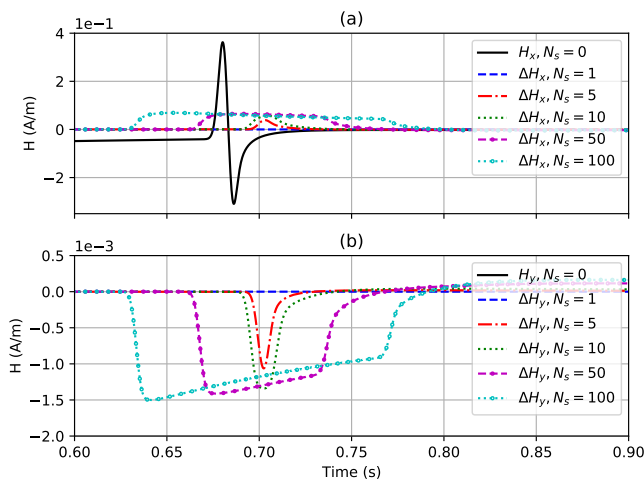
FIGURE 25. (a) H_x, (b) H_y, recorded at top right point P$_{TR}$ in Fig. 15.
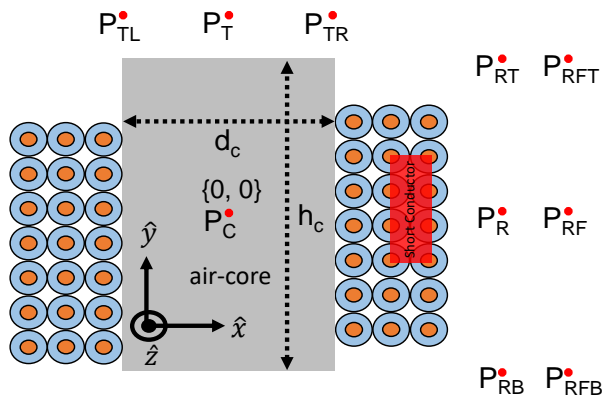
FIGURE 26. Red points indicate the location of H-field sensors relative to center of the air-core (gray rectangle) reactor at point P$_C$= {0, 0}, where
P$_{RB}$= {$r_c + 3d_i + 10r_w$, $-h_c/2$}, P$_{RT}$= {$r_c + 3d_i + 10r_w$, 0},
P$_{RT}$= {$r_c + 3d_i + 10r_w$, $h_c/2$}, P$_{RFB}$= {$2r_c + 3d_i$, $-h_c/2$},
P$_{RF}$= {$2r_c + 3d_i$, 0}, P$_{RFT}$= {$2r_c + 3d_i$, $h_c/2$},
P$_{TL}$= {$-r_c$, $h_c/2 + 10r_w$}, P$_T$= {0, $h_c/2 + 10r_w$}, and
P$_{TR}$= {r_c, $h_c/2 + 10r_w$}. The short conductor (red rectangle) has dimensions $4r_w \times h_s$ with corners at {$r_c + 1.5d_i$, $-h_s/2$} and
{$r_c + 2.5d_i$, $+h_s/2$}; it is inserted on the right between winding layers $m = 2$ and $m = 3$, to induce transient fault currents.

above numerical experiments and record the H-field at the designated points; results are shown in Fig. 27 thru Fig. 36. As can be observed, the trends for $N_{wl} = 3$ are similar to the $N_{wl} = 1$ case, with the main difference being that the $\Delta H_x, \Delta H_y$ deviations are generally smaller compared to the ambient magnetic field; this result makes sense intuitively, given that we increased the number of healthy turns compared to shorted turns.
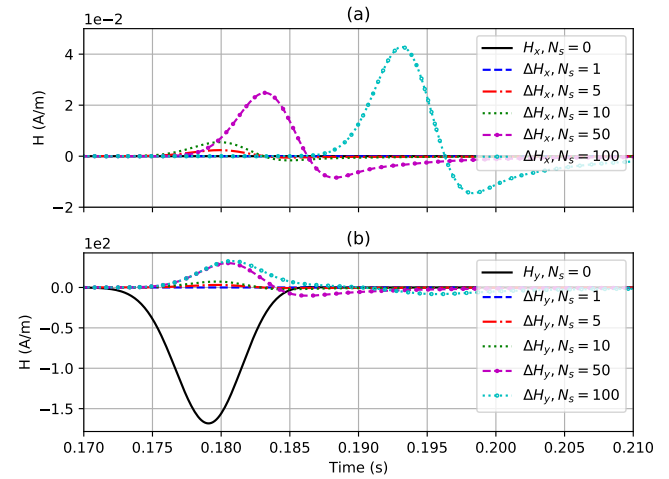
FIGURE 27. (a) H_x, (b) H_y, recorded at the center of reactor, at point P$_C$ = {0,0} shown in Fig. 26. In Fig. 27 thru Fig. 36, the solid black line is the H-field value in normal operation, and dotted/dashed colored lines are the change in H-field value across normal and faulty operations defined in (16).
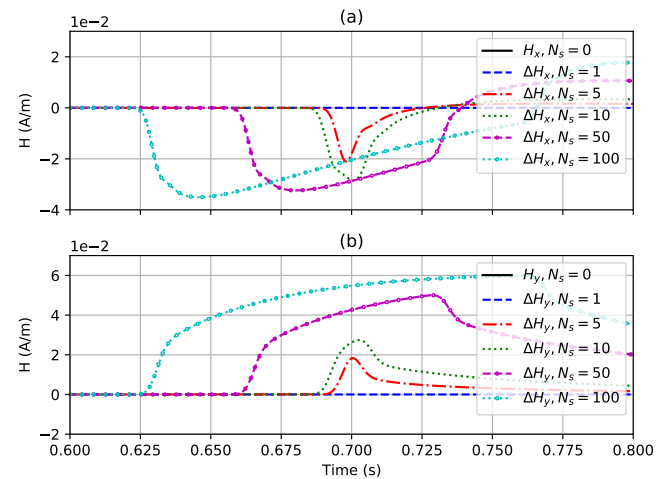
FIGURE 28. (a) H_x, (b) H_y, recorded at right bottom point P$_{RB}$ in Fig. 26.

In light of the above observations, the time-varying H-field emissions across normal vs. faulty operations may be exploited to remotely sense and detect transient fault events due to inter-turn shorts. The simulation methodology described herein may be used to quantify the magnetic field profile as a function of space, time, and reactor parameters, to inform the placement and sensitivity of sensors. A possible detection strategy may include exploration of signal processing and machine learning algorithms for application to the real-time
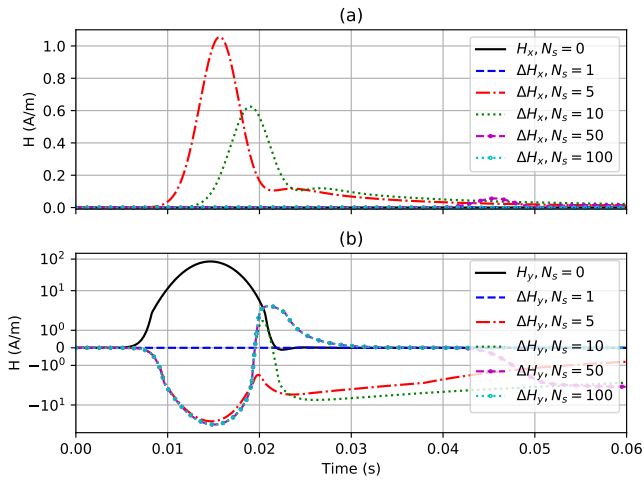
FIGURE 29. (a) H_x, (b) H_y, recorded at the right point P$_R$ in Fig. 26.
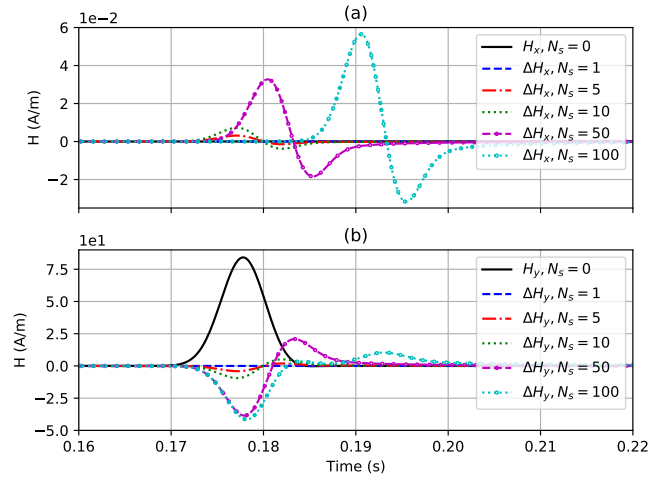
FIGURE 32. (a) H_x, (b) H_y, recorded at far right point P$_{RF}$ in Fig. 26.
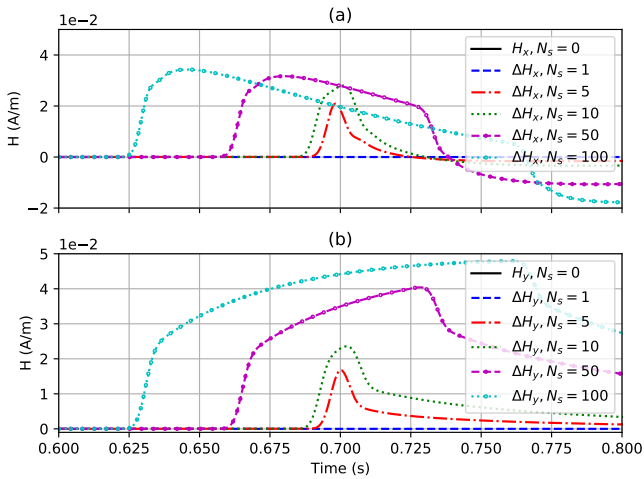
FIGURE 30. (a) H_x, (b) H_y, recorded at right top point P$_{RT}$ in Fig. 26.
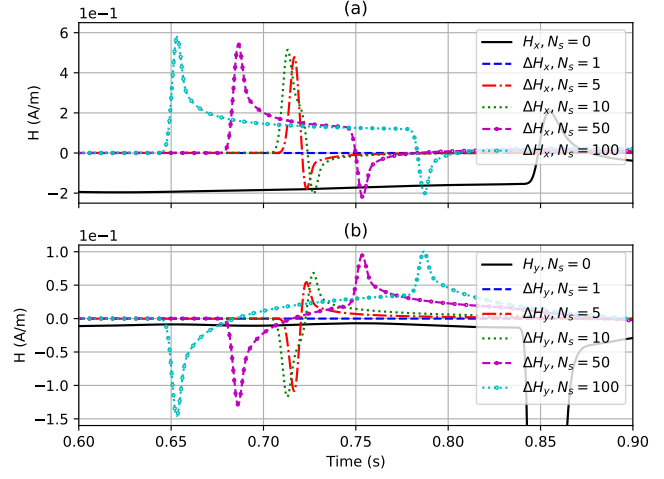
FIGURE 33. (a) H_x, (b) H_y, recorded at far right top point P$_{RFT}$ in Fig. 26.
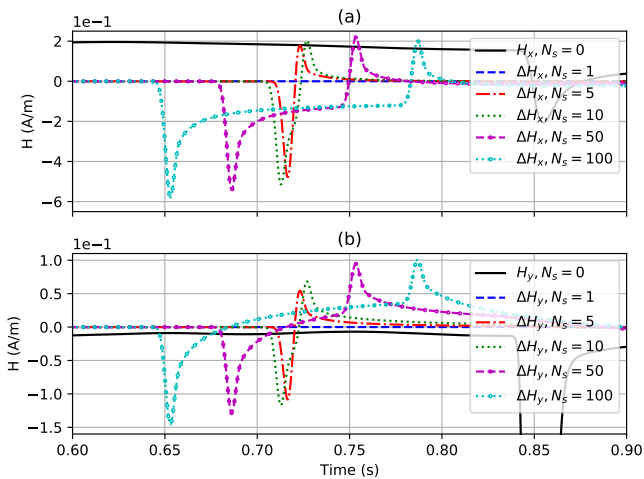
FIGURE 31. (a) H_x, (b) H_y, recorded at far right bottom point P$_{RFB}$ in Fig. 26.
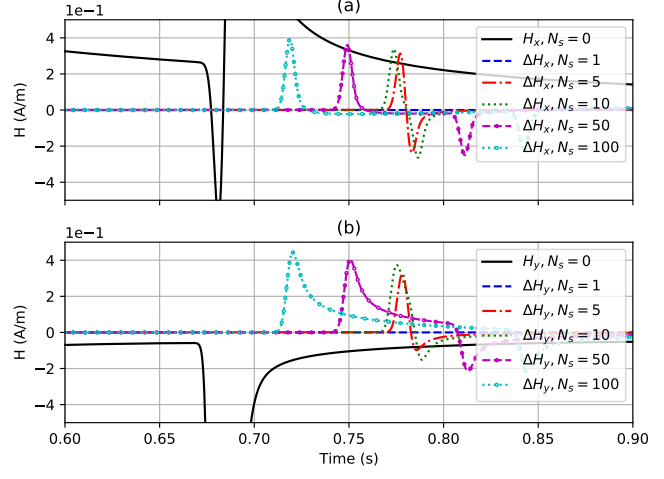
FIGURE 34. (a) H_x, (b) H_y, recorded at top left point P$_{TL}$ in Fig. 26.
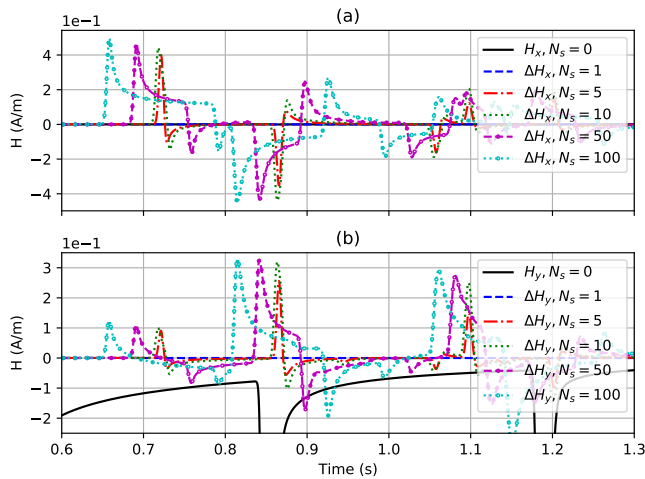
FIGURE 35. (a) H_x, (b) H_y, recorded at top point P_T in Fig. 26.
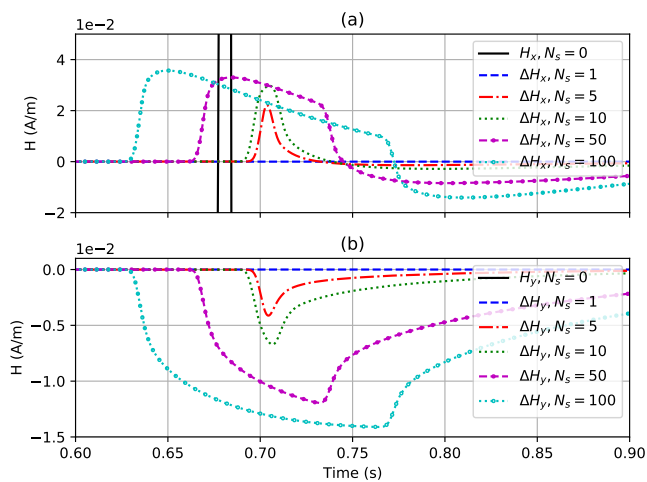
FIGURE 36. (a) H_x, (b) H_y, recorded at top right point P_{TR} in Fig. 26.

detection of transient fault information that may be embedded in the H-field emissions.

V. CONCLUSION

We presented a CEM modeling methodology for estimation of transient fault currents and remote sensing of fault events due to inter-turn shorts in 3D air-core reactors, through a magneto quasi-static approximation in 2D FDTD. An equivalent circuit model of the 3D reactor in normal operation was developed to correlate and scale the MQS 2D FDTD model. The FDTD model was used to compute the transient fault current due to inter-turn shorts. As a demonstration of the proposed CEM modeling methodology, we simulated remote sensing a transient fault event by computing the H-field emissions of a reactor with realistic parameters, compared the transient fault characteristics embedded in the magnetic field signals at several locations around the reactor over time, and suggested some possible strategies for detecting fault events based on signal deviations across normal and faulty

operations.

Some topics of future research may include *(1)* applying signal processing and machine learning algorithms to the emitted H-field signals for real-time detection of transient fault events and locations in the reactor, *(2)* extending the proposed methodology to MQS 3D FDTD, *(3)* exploring methods other than FDTD; e.g., time-domain finite element method (FEM) or transmission line modeling (TLM) method, and *(4)* modeling magnetic-core reactors with hysteresis, where μ_r is a non-linear function of H.

REFERENCES

[1] Schweitzer Engineering Laboratories (SEL). Company website. Pullman, WA, accessed August 17, 2020. https://selinc.com/.

[2] IEEE standard for requirements, terminology, and test code for dry-type air-core series-connected reactors. IEEE Std C57.16-2011 (Revision of IEEE Std C57.16-1996), pages 1–127, 2012.

[3] Kevin Damron. Practical considerations and experiences protecting 230 kV shunt air-core reactors banks. In 43rd Annual Western Protective Relay Conference, Spokane, WA, 2016.

[4] A. I. Mohammad, T. Mort, J. Jeter, A. Hoth, J. England, B. K. Johnson, N. Fischer, and K. Damron. Turn-to-turn fault protection for dry-type shunt reactors. In 2018 IEEE/PES Transmission and Distribution Conference and Exposition (T&D), pages 1–5.

[5] Yu Qin and S. A. Sebo. Accurate evaluation of the magnetic field strength of large substation air-core reactor coils. IEEE Transactions on Power Delivery, 13(4):1114–1119, 1998.

[6] C. R. Sullivan. Optimal choice for number of strands in a litz-wire transformer winding. IEEE Transactions on Power Electronics, 14(2):283–291, 1999.

[7] Asad Iqbal Mohammad. Turn-to-turn fault protection for air core shunt reactors. Master's thesis, University of Idaho, Moscow, Idaho, USA, 2017.

[8] Z. Dazhou, X. Mingkai, D. Xiuming, F. Zhaoyuan, L. Xiaoping, K. Qingkui, and S. Han. Study for spatial magnetic field distribution of inter-turn short-circuit fault degree in dry air-core reactors. In 2018 13th IEEE Conference on Industrial Electronics and Applications (ICIEA), pages 1332–1336.

[9] M. Irhoumah, R. Pusca, E. Lefevre, D. Mercier, R. Romary, and C. Demian. Information fusion with belief functions for detection of interturn short-circuit faults in electrical machines using external flux sensors. IEEE Transactions on Industrial Electronics, 65(3):2642–2652, 2018.

[10] R. Romary, R. Pusca, J. P. Lecointe, and J. F. Brudny. Electrical machines fault diagnosis by stray flux analysis. In 2013 IEEE Workshop on Electrical Machines Design, Control and Diagnosis (WEMDCD), pages 247–256, Paris, France, 2013.

[11] B. Vaseghi, N. Takorabet, and F. Meibody-Tabar. Transient finite element analysis of induction machines with stator winding turn fault. Progress In Electromagnetics Research, PIER 95, pages 1–18, 2009.

[12] C. Zeng, S. Huang, Y. Yang, and D. Wu. Inter-turn fault diagnosis of permanent magnet synchronous machine based on tooth magnetic flux analysis. IET Electric Power Applications, 12(6):837–844, 2018.

[13] M. Dai, A. Keyhani, and T. Sebastian. Fault analysis of a PM brushless DC motor using finite element method. IEEE Transactions on Energy Conversion, 20(1):1–6, 2005.

[14] O. A. Mohammed, Z. Liu, S. Liu, and N. Y. Abed. Internal short circuit fault diagnosis for pm machines using fe-based phase variable model and wavelets analysis. IEEE Transactions on Magnetics, 43(4):1729–1732, 2007.

[15] K. S. Yee. Numerical solution of initial boundary value problems involving maxwell's equations in isotropic media. IEEE Transactions on Antennas and Propagation, Ap14(3):302, 1966.

[16] Allen Taflove and Susan C. Hagness. Computational electrodynamics: the finite-difference time-domain method. Artech House, Norwood, 3rd edition, 2005.

[17] Dennis M. Sullivan. Electromagnetic Simulation Using the FDTD Method. Wiley-IEEE Press, 1st edition, 2000.

[18] Jian-Ming Jin. The finite element method in electromagnetics. John Wiley & Sons Inc., Hoboken. New Jersey, 2014.

[19] Richard Holland. Finite-difference time-domain (FDTD) analysis of magnetic diffusion. IEEE Transactions on Electromagnetic Compatibility, 36(1), 1994.

[20] R. Holland. FDTD analysis of nonlinear magnetic diffusion by reduced c. IEEE Transactions on Antennas and Propagation, 43(7):653–659, 1995.

[21] Mehmet Burak Ozakin and Serkan Aksoy. Application of magneto-quasi-static approximation in the finite difference time domain method. IEEE Transactions on Magnetics, 52(8):1–9, 2016.

[22] M. Clemens and T. Weiland. Numerical algorithms for the FDiTD and FDFD simulation of slowly varying electromagnetic fields. International Journal of Numerical Modelling: Electronic Networks, Devices and Fields, 12(1-2):3–22, 1999.

[23] Jan De Moerloose, Trevor W. Dawson, and Maria A. Stuchly. Application of the finite difference time domain algorithm to quasi-static field analysis. Radio Science, 32(2):329–341, 1997.

[24] C. M. Furse and O. P. Gandhi. Calculation of electric fields and currents induced in a millimeter-resolution human model at 60 Hz using the fdtd method. Bioelectromagnetics, 19(5):293–9, 1998.

[25] Hermann A. Haus and James R. Melcher. Electromagnetic fields and energy. Prentice Hall, Englewood Cliffs, New Jersey, 1989.

[26] Canonical. Ubuntu Linux Operating System, ver. 18.04.4 LTS, accessed June 12, 2020. https://ubuntu.com/download/desktop.

[27] Intel Corporation. Intel Core i7-7600U Processor @ 2.80 GHz, accessed June 8, 2020. https://ark.intel.com/content/www/us/en/ark/products/97466/intel-core-i7-7600u-processor-4m-cache-up-to-3-90-ghz.html.

[28] Clayton R. Paul. Inductance: Loop and Partial. John Wiley & Sons, Inc., Hoboken, New Jersey, 2010.

[29] C. A. Balanis. Advanced Engineering Electromagnetics. John Wiley Sons, Inc., USA, 2nd edition, 2012.

[30] Alan V. Oppenheim, Alan S. Willsky, and S. Hamid Nawab. Signals and Systems. Prentice Hall, Upper Saddle River, N.J., 2nd edition, 1996.

[31] Ata Zadehgol. A semi-analytic and cellular approach to rational system characterization through equivalent circuits. International Journal of Numerical Modelling: Electronic Networks, Devices and Fields, 29(4):637–652, 2016.

[32] Ata Zadehgol. SHF: SMALL: A novel algorithm for automated synthesis of passive, causal, and stable models for optical interconnects. National Science Foundation (NSF) Award #1816542. Proposal submitted on 11/15/2017. Grant period: 10/1/2018-9/30/2021. https://nsf.gov/awardsearch/showAward?AWD_ID=1816542&HistoricalAwards=false.

[33] Walloon Region and et al. ONELAB: Open Numerical Engineering LABoratory, accessed August 17, 2020. http://onelab.info/wiki/ONELAB.

A. ZADEHGOL (SM'16 - M'07) received the B.S. degree in electrical engineering from the University of Washington, in 1996, the M.S. degree in electrical and computer engineering (ECE) from the University of California at Davis, in 2006, and the Ph.D. degree in ECE from the University Illinois at Urbana/Champaign, in 2011. He joined the University of Idaho, in 2014, with more than a decade of experience in advanced microelectronics industry, where he is currently an Associate Professor of ECE, and the director of the Applied Computational Electromagnetics and Signal/Power Integrity (ACEM-SPI) group. His research interests include computational electromagnetics and its various applications in low-frequency to THz electronic systems. His work has been recognized through research grants from the National Science Foundation, NASA, Micron Technology Inc., and Schweitzer Engineering Laboratories, the IEEE TCPMT best poster-paper award, and University of Idaho's Presidential Mid-Career Award. Dr. Zadehgol is a professional engineer licensed in Idaho State.

H. LEI (S'14 - M'16) received the B.E. degree in Electrical Engineering from Huazhong University of Science and Technology, Wuhan, China, in 2011, and the Ph.D. degree in Electrical Engineering from Texas A&M University, College Station, TX, USA, in 2016. He has been an Assistant Professor in the Department of Electrical and Computer Engineering at the University of Idaho, Moscow, ID, USA, since 2017. He was an Assistant Professor at Jackson State University, Jackson, MS, USA, from 2016 to 2017. His industry experience includes two internships at Entergy Corporation, in 2012 and 2014, respectively. His research interests include power system reliability modeling and analysis, state estimation, substation automation, and power system protection. In 2018, he received the Prize Paper Award in the IEEE Power and Energy Society (PES) Technical Committee on Analytical Methods in Power Systems (AMPS).

B. K. JOHNSON (SM'06) received his doctoral degree in EE at the University of Wisconsin-Madison in 1992. He is the Schweitzer Engineering Laboratories Endowed Chair in Power Engineering and a Professor in the University of Idaho ECE Department. His interests include power systems applications of power electronics, power system protection, and power system transients. Dr. Johnson is a registered professional engineer in the State of Idaho.

• • •